Valveless microliter combustion for densely packed arrays of powerful soft actuators

Ronald H. Heisser[a], Cameron A. Aubin[a], Ofek Peretz[b], Nicholas Kincaid[a], Hyeon Seok An[a], Elizabeth M. Fisher[a], Sadaf Sobhani[a], Perrine Pepiot[a], Amir D. Gat[b], and Robert F. Shepherd[a,1]

[a]Sibley School of Mechanical and Aerospace Engineering, Cornell University, Ithaca, NY 14853; and [b]Faculty of Mechanical Engineering, Technion–Israel Institute of Technology, Haifa 3200003, Israel

Edited by Herbert Shea, Ecole Polytechnique Federale de Lausanne, Lausanne, Switzerland and accepted by Editorial Board Member John A. Rogers August 21, 2021 (received for review April 6, 2021)

Existing tactile stimulation technologies powered by small actuators offer low-resolution stimuli compared to the enormous mechanoreceptor density of human skin. Arrays of soft pneumatic actuators initially show promise as small-resolution (1- to 3-mm diameter), highly conformable tactile display strategies yet ultimately fail because of their need for valves bulkier than the actuators themselves. In this paper, we demonstrate an array of individually addressable, soft fluidic actuators that operate without electromechanical valves. We achieve this by using microscale combustion and localized thermal flame quenching. Precisely, liquid metal electrodes produce sparks to ignite fuel lean methane–oxygen mixtures in a 5-mm diameter, 2-mm tall silicone cylinder. The exothermic reaction quickly pressurizes the cylinder, displacing a silicone membrane up to 6 mm in under 1 ms. This device has an estimated free-inflation instantaneous stroke power of 3 W. The maximum reported operational frequency of these cylinders is 1.2 kHz with average displacements of ∼100 μm. We demonstrate that, at these small scales, the wall-quenching flame behavior also allows operation of a 3 × 3 array of 3-mm diameter cylinders with 4-mm pitch. Though we primarily present our device as a tactile display technology, it is a platform microactuator technology with application beyond this one.

soft electronics | haptics | combustion | microactuator | microfluidics

Through the senses, human beings constantly gain rich information about the external world; ultimately, everything one knows comes from what one first learns through one's sense powers (1). Though sight is generally considered to be our strongest sensorial asset, touch (pressure, pain, vibration, temperature, etc.) intimately connects us with our nearby environment and our own bodies. Touch is, perhaps, more necessary for survival than any other sense (2–8). It is unsurprising, then, that our skin is our bodies' largest organ (9, 10), comprising in part a diverse array of mechanoreceptive organelles, allowing people to feel skin deformations of different types, durations, and intensities (11). For example, human fingertips have over 200 mechanoreceptive units per square centimeter (10), perceiving static deformations of down to 0.1 mm (12) and vibrations of up to 400 Hz (10, 13).

Despite the importance of touch, our visual and auditory senses dominate the experience of digital information. The most proliferate form of haptic actuation is vibrotactile, but this technique does not allow the type of displacement and persistence of touch required to provide a natural experience. Vibrations alone cannot meaningfully recreate the pressure felt from a bag on the shoulders or the impact of a ball caught in the hands. Because of this lack of haptic experience, at least two societal needs remain unfulfilled: artificial touch recreation in immersive virtual reality (VR) and braille displays that compete with analogous visual media. For braille, specifically, there are no full-page, affordable, portable, refreshable displays on the market (14).

The dearth of available tactile display options is not from lack of trying; manufacturing arrays of actuators at the size and density suitable for reading computer information from a tactile screen requires reducing actuator volume, weight, power draw, and cost, all together. The diverse set of designs conceived to achieve this haptic challenge have employed an equally numerous suite of physical principles, and each actuation method has presented its own failure mode (14). For example, thermal actuators usually take seconds (without thermal management accessories) (15) to finish a work loop because of heat transport limitations (16). Pulsed electromagnetic systems suffer from low actuation forces and interference between individual actuators (crosstalk) when made close to the size of a braille dot (17). Piezoelectric devices have large production costs at scale (HyperBraille systems cost ∼$50,000), also needing long cantilevered geometries that impede their ability to be densely arranged (14, 18).

Fluidic elastomer actuators (FEAs) displace rubber forms with liquids and gases, showing promise as dense actuator arrays because of their manufacturing simplicity and favorable mechanical characteristics (19). An elastomeric membrane ∼1 mm in diameter can displace more than 0.5 mm as was previously shown by ref. 20 in which a 1.5-mm diameter viscoelastic membrane displaced 0.56 mm in about 1 s. Beyond simplicity, these soft haptic devices also have the convenient ability to conform to complex body shapes (21). For example, HaptX has developed a commercial, tethered VR glove technology that integrates 130 individually addressable fluidic actuators into each glove (22). This paper's lead author has experienced this technology and testifies to its natural feel (23). As designed, the glove's microfluidic channels

Significance

Even in the rapidly accelerating digital age, the portable, electronic tactile display remains an unsolved actuation technology challenge. The design requirements associated with manufacturing arrays of closely spaced, small actuators are notoriously difficult to satisfy, shown by how currently available actuation strategies fail when implemented at the scale of braille dots. Through experiments with a less common actuation method, microliter combustion in elastomers, we find that hyperelastic membranes can be forcefully and quickly displaced. Without valves, we can pack actuators more closely together to introduce a potential pathway toward powering a practical, portable, electronic haptic display system.

Author contributions: R.H.H., E.M.F., S.S., P.P., A.D.G., and R.F.S. designed research; R.H.H., C.A.A., O.P., N.K., H.S.A., and R.F.S. performed research; R.H.H., O.P., N.K., P.P., A.D.G., and R.F.S. analyzed data; R.H.H., C.A.A., O.P., N.K., H.S.A., E.M.F., S.S., P.P., A.D.G., and R.F.S. wrote the paper; and R.H.H. designed and fabricated devices.

Competing interest statement: R.F.S., C.A.A., and R.H.H. are coauthors on a patent filed by Cornell University on August 19, 2020, titled "Microscale Combustion for High-Density Soft Actuation," claiming priority to US Provisional Application No. 62/888,836, filed on August 19, 2019, by the same authors.

This article is a PNAS Direct Submission. H.S. is a guest editor invited by the Editorial Board.

[1]To whom correspondence may be addressed. Email: rfs247@cornell.edu.

This article contains supporting information online at https://www.pnas.org/lookup/suppl/doi:10.1073/pnas.2106553118/-/DCSupplemental.

Published September 23, 2021.

are tethered to a large box housing a pump and many valves, limiting the user's range of motion. One major deficiency of FEAs is how the system scales with actuator number density: there is generally a linear relationship between the number of valves and actuators. As electromechanical valves are themselves actuators, the size, weight, power, and cost (SWaP-C) requirements of FEA arrays soon become untenable for portable tactile display systems. For example, the most popular valve choice for FEAs is the Parker X-Valve, with dimensions of $7.87 \times 23.37 \times 12.30$ mm^3 at a unit cost of ~$40 (24); if a single, six-dot braille cell ($\sim 6 \times 10 \times 10$ mm^3) was controlled by six valves, that is, one valve per actuator, the array of valves would take up 18.4 times the cell area and cost $240 (14). Though there are multiplexing solutions to the valving challenge (25), we are currently unaware of any high-resolution tactile interaction being enabled by these methods.

Counterintuitively, microscale combustion could provide an alternative actuation motif for haptic arrays, given its own engineering tradeoffs. Combining high-energy density fuels (26, 27) with small-volume mechanical elements results in a potentially safe and enduring actuation mechanism. Previously, microscale combustion research primarily focused on replacing batteries with high–power density micro-electromechanical systems (MEMS) thermoelectric generators (28). These systems may have failed to become practical because of unwanted flame extinction, thermal degradation, and frictional wear (29). More recently, combustion has been used in FEAs for macroscale soft robots and pumps (30–34). A spark ignites a combustible gas mixture that rapidly heats the product gas and expands the soft FEA cavity to move a robot or separate fluid. This research direction, however, has not been previously expanded into the realm of small gas-powered FEAs (35).

In this paper, we make two contributions: 1) the use of combustion in microliter-scale FEAs for powerful, high-stroke, millimeter-scale actuations and 2) the exploitation of rapid thermal quenching at these scales to individually actuate fluidically coupled arrays without valving. As we no longer need valves, we can space the actuators more closely because their flow and electrical control components occupy less area than the actuator footprint. Primarily composed of molded silicone and microfluidic liquid metal (LM) traces, our design is an inexpensive, thin rubber sheet that provides more favorable SWaP-C scaling than prior FEA systems. We elementally characterize our device's mechanical performance as a general microactuation strategy. As tactile display systems represent one of the oldest, broadest, and most contemporary microactuator research initiatives, we focus our discussion and demonstration on this system's potential to serve a similar purpose.

Results

Single-Cylinder Actuator Design Rationale. Fig. 1*A* shows a rendered schematic of our single-cylinder actuator. A 2-mm thick, molded layer of polydimethylsiloxane (PDMS; Sylgard 184, Electron Microscopy Sciences, Inc.) contains the geometries of the actuation cylinder, gas delivery channels, and LM electrode channels. A 1-mm thick bottom layer seals the cylinder and channels. Including the outer substrate, this device has dimensions of $40 \times 65 \times 3$ mm^3; we include excess PDMS at the base layer for ease of handling. We bond a 7-mm diameter, 0.5-mm thick hyperelastic (Ecoflex 00–30, Smooth-On, Inc.) membrane to the top of the cylinder with a silicone epoxy (Sil-Poxy, Smooth-On, Inc). Assembly steps can be found in *SI Appendix*, *Single Cylinder Actuator* and *Arrayed Actuator*. Our choice of PDMS in these actuators stems from its thermal stability (silicones can withstand constant temperatures above 150 °C) (30, 36), large strain to failure, toughness, and cycle lifetime (30, 33, 37). PDMS has previously been shown to survive the elevated temperatures and pressures of larger, soft, combustive actuators (30, 32, 33).

To embed the spark gap electrodes, we inject liquid gallium (single actuator) or EGaIn (arrayed actuator) into the PDMS substrate (Fig. 1 *A*, *Inset*). These LM options perform equally well in both cases and are useful to retain high device elasticity. LM also simplifies our device construction, as it functions both as the spark gap electrodes and internal conductive traces. Fortunately, the oxide layer that forms on the LM surface helps stabilize the exposed liquid metal electrode surface during bending and combustion (38).

While LM has a higher resistivity ($\rho_{Ga} \sim 10^{-7}\ \Omega$ m) than metals typically used in conventional circuitry ($\rho_{Cu} \sim 10^{-8}\ \Omega$ m) (38), it is still a good choice for our design. The higher resistivity is less important, as our device is primarily electrostatic; only electric breakdown causes charge to flow. Specifically, considering the parallel plate capacitance C of two closely spaced flat wire ends, the time to spark formation can be estimated as $t_c \sim RC$ (R is resistance). Then, copper traces will take 12% the time to charge as gallium traces since $\rho_{Cu}/\rho_{Ga} = 0.12$. Assuming a total input impedance of 1 kΩ, $t_{c,Ga} \sim 1$ ns. Therefore, the relatively low LM conductivity does not impact the practical operation of this device, making LM an overall better design choice than solid metallic conductors. As repeated electrostatic discharges tend to erode and foul solid electrodes (39), LM provides an additional benefit in that the electrodes could potentially heal themselves or be replenished by injecting more LM.

Actuator Operating Principle. Our actuator functions similarly to that of pistons in an internal combustion engine (ICE)—a spark ignites a gaseous reactant mixture to heat and rapidly expand gas to perform work (40). For our soft ICE, we chose to use methane and oxygen, which globally react according to Eq. **1**, and from this reaction, release 55 kJ of heat per gram of methane consumed (includes exothermic water condensation, *SI Appendix*, *Actuator Stroke Efficiency*):

$$CH_4 + 2O_2 \rightarrow CO_2 + 2H_2O(l). \quad [1]$$

At the instantaneously high pressures generated by this reaction, the open exhaust port restricts but does not prevent gas outflow as the membrane stretches upward. Schlieren imaging of exhaust flow (*SI Appendix*, Fig. S7) shows the exhaust gas pluming after actuation begins. Though prior research has shown that passive elastomeric check valves can trap exhaust gases only during combustion (30), our simpler design is easier to fabricate at small scales. Therefore, we sacrifice efficiency for architectural simplicity and high-resolution actuator density. Individual actuation events are controlled by ignition through the LM electrodes.

Experimental Performance Characterization. The free inflation (Fig. 1*B*) and deflation of the hyperelastic membrane provides a visual basis to estimate the actuator's mechanical performance envelope. The energy released during combustion depends on the proportion of methane present in the mixture, expressed by the equivalence ratio Φ (40):

$$\Phi = \frac{\left(m_{fuel}/m_{oxidizer}\right)_{actual}}{\left(m_{fuel}/m_{oxidizer}\right)_{stoich}}, \quad [2]$$

where m refers to the mass. When all fuel and oxidizer convert into products, the reaction is considered stoichiometric: $\Phi = 1$. Combustion reactants at $\Phi < 1$ are referred to as lean mixtures. We report actuator performance for $\Phi \in [0.20, 0.34]$. We estimated the membrane stretch λ_p and normalize volume change $\Delta V(t) V_0^{-1}$ over the different Φ's using high-speed video (Fig. 1 *C* and *D*). At $\Phi = 0.34$, $\Delta V_{max} V_0^{-1} = 3.05$ and $\lambda_p = 4.1$. These quantities contribute to a first order energy output estimate, the total membrane stroke work of combustion, W_s, defined below as the (neo-Hookean) strain energy Ψ increased in the membrane from combustion (41–43):

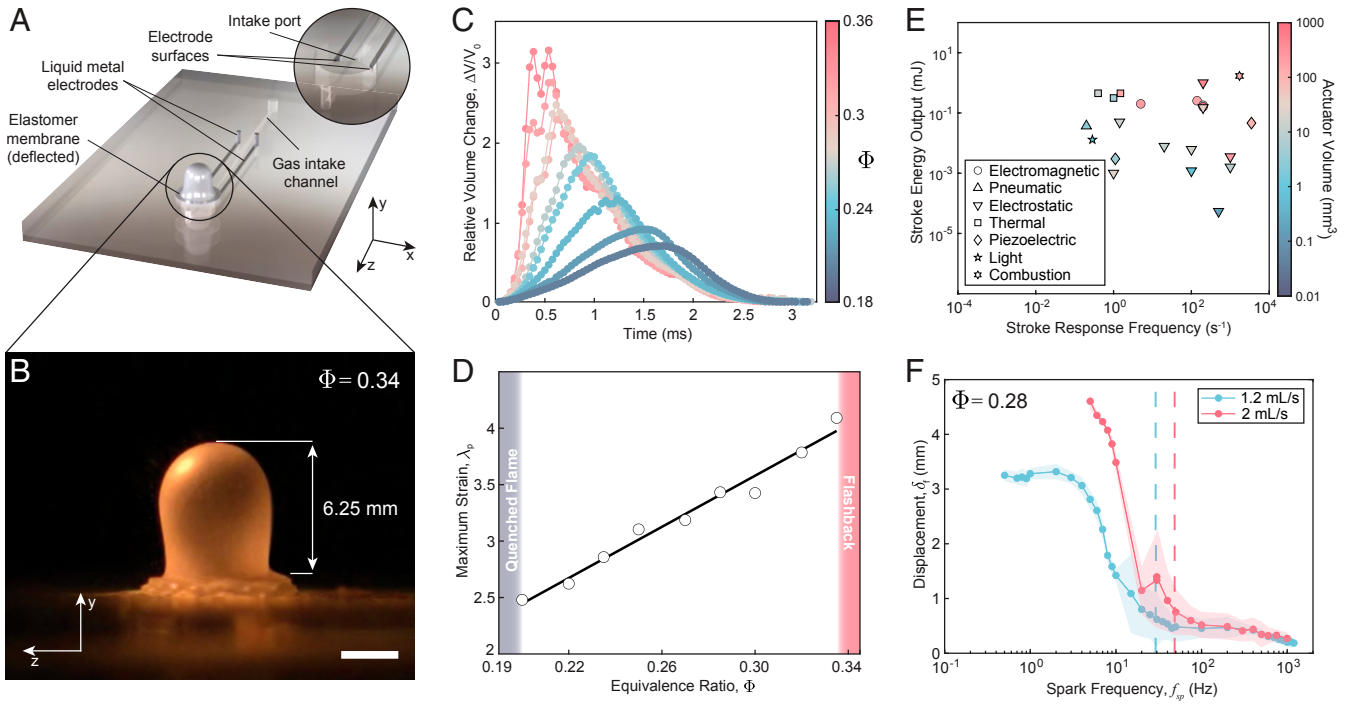

Fig. 1. Valveless microliter combustion repeatably and powerfully displaces hyperelastic membranes. (*A*) A rendering of the single-cylinder (5-mm diameter, 2-mm depth) actuator details the construction and intra-cylinder arrangement of gas ports and spark ignition electrodes. The LM electrodes terminate at the cylinder edge (*Inset*), their exposed surfaces forming the spark gap. (*B*) High-speed photography captures fast dynamics of single-cylinder actuation strokes. (Scale bar: 3 mm.) (*C*) Image analysis from high-speed videos shows that methane–oxygen combustion reaction rates increase sharply as Φ rises. (*D*) Maximum membrane stretch ratios estimated from the same video data used in *C* are above 400%. (*E*) Energy output, response time (stroke response frequency), and actuator volume metrics taken from literature capture the approximate power densities of other reported tactile display systems. (*F*) Continuous reactant replenishment enables high spark frequencies to trigger high-frequency actuations up to 1.2 kHz. Vertical lines depict spark frequency equal to the theoretical rate at which the gas flow refills the cylinder. Shading shows the SD of each measurement.

$$W_s = \Psi = \frac{\mu}{2}\left(2\lambda_p^2 + {}^1\!/\!_{\lambda_p^4} - 3\right)Ah. \qquad [3]$$

From our analysis, we estimate that this device produces a maximum stroke work $W_s = 1.7$ mJ and maximum instantaneous stroke power output $P_s = 2.9$ W. We report power in this manner to highlight the explosive energy release during actuation. For example, the average velocity of the strongest upward stroke (Fig. 1*B*) is 10.8 m · s^{-1}. A power estimate averaged over cycles of actuation would include idling periods and is significantly lower. Reactant gas flowing at 1.2 mL · s^{-1} (Φ = 0.28), sparking at 10 Hz, produces a power output of ∼2.7 mW. For tactile display applications, the stroke power more accurately reflects the overall performance since it incorporates both actuator energy output and the response time into one number; the latter measure is also important for future, higher fidelity VR haptic feedback technologies. We set our results in context through Fig. 1*E*, compiling estimated stroke power outputs from peer-reviewed publications that report sufficient experimental data (geometry, force, displacement, and response time) (16, 17, 19, 20, 44–60). Consult *SI Appendix*, *Details on Actuator Performance Comparison* and Table S1 for literature comparison details.

We obtained the experimental actuator frequency response curves shown in Fig. 1*F* by sweeping sparking frequencies up to 1.2 kHz while maintaining constant input gas flow rate and stoichiometry. Even at these high frequencies, we were able to measure displacements of >100 μm despite the reduced reactant gases present in the cylinder. For comparison, a single spark plug in an ICE running at 3,000 rpm ignites new fuel–air mixtures at 25 Hz. We far exceed these operational frequencies as our system does not have valve-timed processes. New gas enters the cylinder during the current actuation and quickly becomes available for the next ignition because the electric discharge path is located directly in front of the intake port (Fig. 1 *A*, *Inset*). As we limited our premixed fuel flow rates for experimental safety purposes, we could likely increase the actuation frequencies beyond 1.2 kHz for less safety-constrained applications.

The vertical lines in Fig. 1*F* represent the frequencies at which reactant gas can refill the cylinder volume for two experimental volumetric flow rates Q of 1.2 and 2 mL · s^{-1}. Ideally, all sparking frequencies f_{sp} less than the corresponding "filling frequency" $f_f = Q\,V_0^{-1}$ would produce displacements of the same amplitude. In reality, we observe both a drop in the average displacement amplitude and an increase in the peak displacement variance for $f_{sp} < f_f$ (Fig. 1*F*). Further investigation of individual measurements taken at intermediate frequencies (tens of Hertz) reveals a stable sawtooth pattern (*SI Appendix*, *Experimental Frequency Response Analysis* and Fig. S14). We proceeded to develop a linearized fluid–structure interaction (LFSI) model to rationalize this experimental anomaly (assuming uniform, instantaneous species mixing). This model did capture many features of our frequency response experiments, even showing a subtle displacement variance ∼0.1× the magnitude of experimental measurements. From our initial simulations, we believe that some ambient or exhaust gas is sucked back through the exhaust port into the cylinder due to a momentary negative pressure differential generated by rapid gas cooling and membrane over-deflection into the chamber during deflation (*SI Appendix*, *Linearized Fluid-Structure Interaction Model (LFSI)*). Further analysis incorporating inlet gas dynamics and nonlinear elasticity may lend a more complete explanation of our experimental observation.

Microliter Fuel–Oxygen Combustion Mechanics. Methane–oxygen combustion plays a dual role in generating our device's powerful actuations. Firstly, using pure oxygen allows for reactant mixtures to have higher energy densities than methane–air mixtures. A stoichiometric methane–air mixture has the same mass of methane as a methane–oxygen mixture at $\Phi = 0.21$. Secondly, the reaction kinetics of fuel–oxygen mixtures result in a faster flame and hotter product gases, as less inert gas is present to absorb heat. Fig. 2*A* supports these intuitions with data from simulations of unconfined laminar methane–air and methane–oxygen flame propagation (61).

Because our actuator cylinder has a relatively high surface-area-to-volume ratio, flame–wall interactions also affect flame propagation behavior. Recent deflagration-to-detonation (DDT) investigations have gained significant insights into how the boundary layer promotes flame acceleration in narrow, closed-end tubes (62–67). To contrast, the first order combustion theory most successfully predicts flame behavior when it is relatively unconfined and moves at the laminar flame speed (Fig. 2*B*). We examine the validity of laminar flame assumptions by comparing experimental data with a laminar flame propagation (LFP) model, further contextualizing our results (Fig. 2*C* and *SI Appendix*, *Laminar Flame Propagation Model (LFP)*). That the experimental data most closely fits the timescales from the LFSI lends credence to our claim that the flame accelerates in the cylinder immediately following ignition.

Design features like asymmetric electrode placement, open port configuration, and a hyperelastic boundary layer limit how precisely current DDT theory can explain our experimental observations. Yet, simulations show transitional flame behavior occurring in tens of microseconds because of narrow tube wall friction (62–65), aligning well with our measurements (63), assuming that in our device the reaction completes no later than when the membrane begins its motion. The simulations also demonstrate the role that internal acoustic reflections play to further the acceleration. We do not claim that detonation occurs in our device; however, higher stoichiometries result in combustions that produce a sharp, loud snap. It is possible that the cylindrical actuator wall encourages constructive acoustic interference in the reacting gas.

The continuous-flow combustion processes we use are prone to flashback in which flames faster than their feed gas velocity proceed upstream toward the fuel source. Flashback in industrial equipment like oil pipelines and oxyacetylene welding rigs poses a serious safety risk, especially when backpropagating flames cause sharp pressure spikes in the gas tanks or fuel lines. Preventing flashback requires a design feature—a flashback arrester—that absorbs enough heat from the flame to cool it below a self-sustainable temperature, terminating the combustion reaction. Sir Humphry Davy discovered a mechanism whereby a propagating flame quenches itself when confined by a metal mesh of sufficiently small pores (68), establishing a principle for the future design of flashback arrestors. The small port geometries naturally exhibit this principle for our lean oxy–methane mixtures. Yet, when $\Phi >$ 0.34, ignition produces stronger flames that proceed backward through the entire device.

Later investigations into porous flame quenching have shown that high-speed flames violate Davy's principle; thick flame arresters with even smaller pores are needed to slow, depressurize, and quench more energetic flames (69). We incorporate this more substantial flame arrestment method into our array prototype (Fig. 3*A*) by embedding a single 1.5-mm thick sintered metal disk (1000840-01-020, Mott Corporation) in the central junction of the fuel channels. The disk also diminishes traveling pressure waves from individual combustions, thus reducing unwanted crosstalk.

Arrayed Actuation System. To translate the single actuator design into a scalable arrayed device, we separate cylinders, electrodes, and gas channels into four layers; putting each of the components under the cylinder frees space on the top layer to bring actuators more closely together. The footprint of each cylinder is larger than the gas and electrode channels, enabling us to directly integrate these components (Fig. 3*B*).

LM electrode channels occupy the bottom two device layers, where one widthwise channel crosses over one lengthwise channel under the center of each cylinder. The high-voltage (HV) control relays are set to normally open, leaving each trace electrically disconnected as the array idles. Individual actuations are triggered by setting the widthwise channel to +V (~2 kV) and the lengthwise channel to ground. Wires that pierce through the bottom of the cylinder into each electrode channel carry charge and cause a spark in front of the fuel intake port (*SI Appendix*, Fig. S3). Thus, we demultiplex the electrical inputs of this system by controlling the voltage of electrode rows and columns, not the individual actuators. To prove this concept, we first verified that each actuator works independently by manually triggering HV relays to ignite fuel in each of the nine cylinders. High-speed video captured individual membrane inflation and deflation cycles (Fig. 3*C* and *SI Appendix*, Fig. S9 and Movie S5).

To produce sustained deformations required for effective tactile displays, we connect our prototype array to a set of magnetically latching pins. We use the HV relays (controlled by an Arduino Uno) to trigger combustion sequences of prescribed braille and English text outputs (Fig. 3*D* and *SI Appendix*, Fig. S10). The transient pressure pulses push the pins upward to remain in a raised state because of the magnetic latches. After each actuation

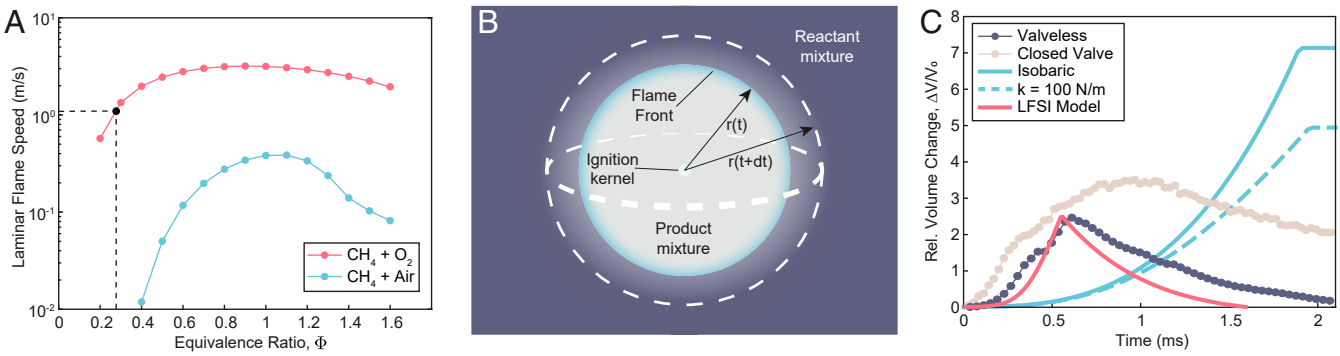

Fig. 2. Microliter methane–oxygen combustion processes deviate from laminar flame theory. (*A*) Simulated flame speed curves compare the speed scales occupied by methane–air and methane–oxygen mixtures. The specified point on the methane–oxygen curve shows the flame speed used for theory–experiment comparison. (*B*) Diagram visualizes flame propagation used to estimate incremental energy addition for the LFP model in *C*, given by the blue lines. (*C*) LFSI and LFP are compared with experimental data taken at $\Phi = 0.28$ (Fig. 1*C*). The valveless experiment is supplemented by an additional "closed valve" experiment in which miniature solenoid valves (X-5–05-S-F, Parker Hannifin Corp.) close off both gas ports.

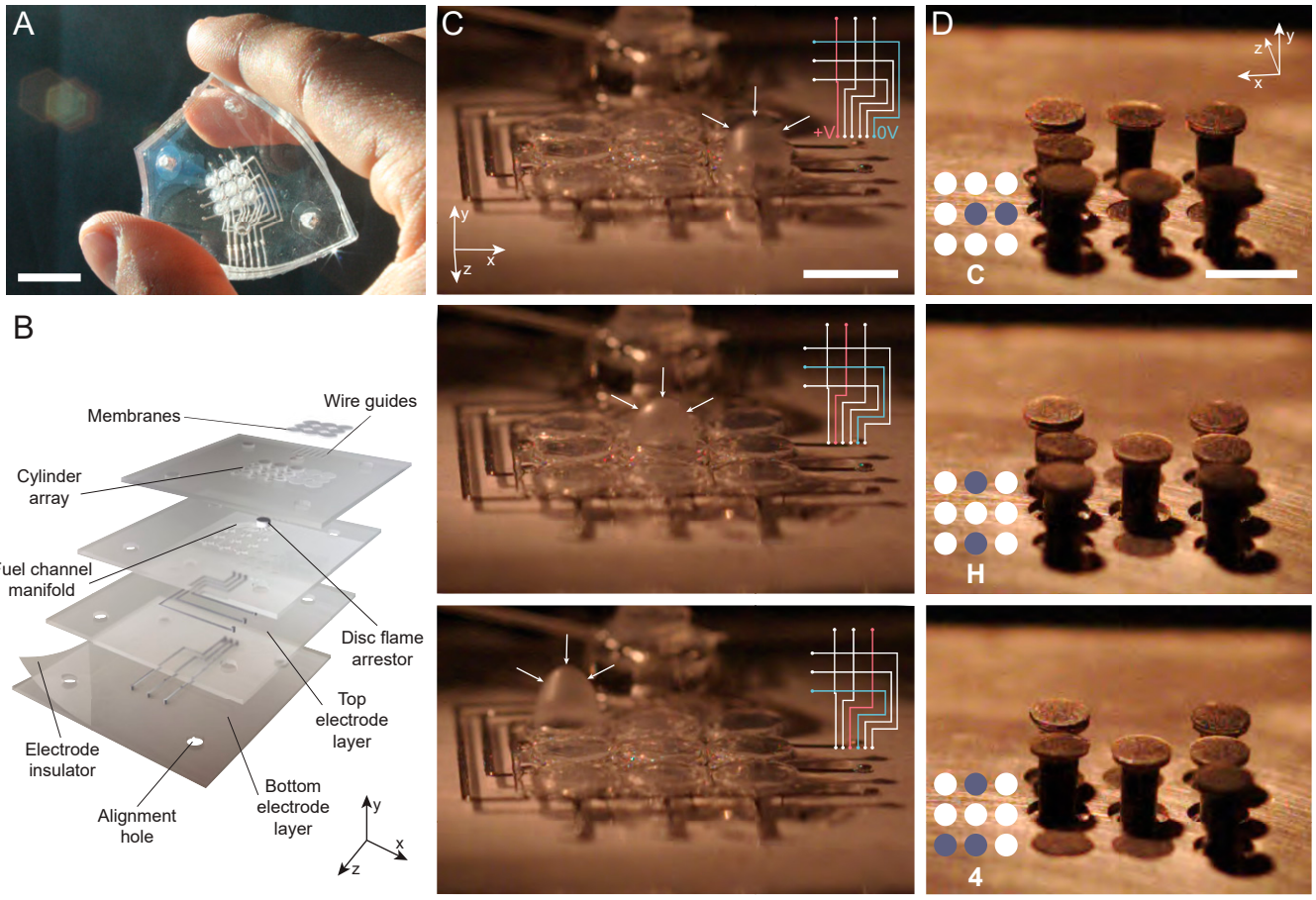

Fig. 3. Design for individually addressable, high-density arrays of soft actuators. (*A*) Arrayed actuator design is compliant (*SI Appendix*, Fig. S1) and biocompatible. (Scale bar: 15 mm.) (*B*) An exploded view visualizes the layer-by-layer device architecture. Array cylinder electrode details can be found in *SI Appendix*, Fig. S3. (*C*) High-speed images show individual operation of different actuators (Movie S5). Two-dimensional diagram of HV demultiplexing traces given in righthand corners. (Scale bar: 5 mm.) (*D*) A tactile display application was demonstrated with an elementary magnetic latching pin array placed directly above membranes. The pins rest in a steel machined plate (*SI Appendix*, Fig. S10). Separate actuation procedures are high-speed recorded, spelling "CH4" in self-reference to the methane which powers this system (Movie S6). All demonstrations were performed at $\Phi = 0.28$. (Scale bar: 5 mm.)

sequence, we reset the raised latching pins by manually pressing them back down. Because the relays were directly connected to the Arduino with no filtering components, leakage currents from electrical breakdown occasionally interfered with the microcontroller clock cycles (*SI Appendix*, *Arrayed Actuator* and *Spark Demultiplex Control Electronics*), artificially increasing the overall array actuation timescale compared to the 5-ms pin motion time.

Discussion

We have designed, manufactured, and characterized an actuation system, simply composed of molded silicone and microfluidic LM traces, that releases energy from microliters of fuel to repeatably generate membrane pulses above 1 kHz up to 2.9 W of power. Our actuator array exceeds the current Pareto front (energy output versus response time) for haptic arrayed actuation technologies. Presently, we can use computer-controlled protocols to actuate individual cylinders in a 3 × 3 array. The toughness and compliance of the materials we use in our device (i.e., silicone and LM) builds upon lessons learned from previous microcombustion work, avoiding the pitfalls of tribological wear and thermal degradation (29). The simplicity of our system architecture gives it potential to be far less expensive than currently available refreshable braille displays (*SI Appendix*, *Design for Scale*).

Core to this system's potential is the elimination of electromechanical fluid control components. The self-quenching behavior of flames at small scales allows us to design a valveless, electronically controlled FEA. It is for this reason that we can reduce the individual actuator footprint and pack actuators more closely. Our reported array prototype has 3-mm diameter cylinders at a 4-mm pitch; we also have preliminary data showing that 1-mm diameter operation is achievable for larger Φ (*SI Appendix*, Fig. S5). Our device is naturally suited to haptics applications because it can conform to complex body geometries. Though combustion produces heat, continuous exhaustion and rapid membrane expansion effectively reduces heat transfer to the cylinder walls, diminishing any device heating over long periods of use. If we use our concept in stretchable electronics applications, the components themselves will undergo stretching, bending, and twisting (*SI Appendix*, Fig. S1). Our piercing spark gap electrode wires, then, are subject to unwanted contact and misalignment. Wicking small amounts of epoxy or ultraviolet-curable resin between the electrodes can effectively bond them to the PDMS substrate and ensure robust spark gap spacing.

In this work, we trigger actuation with sparks because they allow fast actuation frequencies and therefore, higher tactile bandwidths. While miniature HV boost converters can continuously produce over 10 kV with a power draw of ~500 mW, producing HV electric breakdown requires relays that are generally bulkier and costlier than standard switching components (*SI Appendix*, *Spark Demultiplex Control Electronics*). If we can reduce the breakdown voltage to below 1.5 kV, we will also substantially reduce relay size and cost. As there is currently little commercial need for kV-level demultiplexing, recent

breakthroughs in semiconducting and piezoelectric technologies might soon produce more compact solutions (70–72). Resistive and optical MEMS microheaters typically used in on-chip gas sensors should be evaluated for their potential to trigger combustion since they are known to sustain high temperatures (>1,000 °C) and have response times of about 10 ms to 100 ms (73, 74). Novel HV pyroelectric materials may also serve as future compact spark generators (72). Lastly, manipulating the gaseous dielectric breakdown strength by varying reactant species concentrations can provide a means to chemically control actuation at constant electrode tension. The breakdown strengths U_b of atmospheric oxygen and methane between electrodes separated by 1 mm are $U_{b,O2}$ ~1 kV and $U_{b,CH4}$ ~5 kV, respectively (75, 76).

While our actuator has a low stroke efficiency ($\eta_s = 0.71\%$, *SI Appendix, Actuator Stroke Efficiency*), our reported mechanical performance is excellent for the purposes of microactuation; the amount of chemical energy and the reaction rate of combustible fuels at microliter volumes compensate for its low efficiency. Currently, state-of-the-art batteries have energy densities 10 to 100 times lower than hydrocarbons (77). Hydrocarbons are surpassed in specific energy only by some radioactive elements and antimatter (26, 78). Furthermore, to make this device portable, we can use liquid fuels (e.g., butane) and possibly on-board oxygen concentration to provide days of use before refueling (79).

We acknowledge that some may find the thought of being so close to combustible chemicals unsettling, yet we note that billions of liquid butane lighters have rested in people's front pockets since the 1800s, and most every driver willingly sits within a few feet of continuous cyclic combustion reactions, only slightly farther away from gallons of gasoline. With a full-page refreshable braille tablet (*SI Appendix, Design for Scale*), it would take a person ~10^6 page refreshes (using all possible actuators for each refresh) to release the same amount of chemical energy stored in one 15-gallon tank of gasoline. Furthermore, the lithium–ion battery has shown the potential to be unsafe when mismanufactured (80). We do not optimize our preliminary system for efficiency; designers can optimize chamber geometry, gas composition, and membrane properties to use the least fuel for particular applications.

We believe that this system is a strong candidate for powering many technologies beyond haptics. This actuator can be integrated with small power transmission components to make microrobots move quickly and can sit beneath microfluidic devices as simply distributed micropumps for untethered soft machine operation. Antagonistic pairs of actuators could replace small solenoid valves to compactly control higher degree-of-freedom FEAs. For wearable applications, the current array configuration could be scaled to reproduce some transient tactile sensations like wind, raindrops, or a small insect scuttling about one's body.

Materials and Methods

Fabrication. We used soft lithography with three-dimensional, or 3D-printed (Stratasys Objet30 Scholar, VeroBlue photopolymer) molds to produce simple, stacked-layer device prototypes. The layer substrate is molded PDMS (Electron Microscopy Sciences). Molding processes can be replicated at smaller scales with cleanroom microfluidic techniques. The membranes were made by doctor blading Ecoflex 00–30 (Smooth-On, Inc.) onto glass plates. The membrane shear modulus $\mu = 11$ kPa was calculated from previously obtained Ecoflex 00–30 tension test data (81). Either EGaIn (Sigma-Aldrich) or liquid gallium was used for electric traces and electrodes, with no appreciable difference in performance. Liquid gallium electrode traces remained in liquid phase for months after experiments and did not show any appreciable degradation (82). Premixed methane–oxygen gas fueled all combustion processes.

Experiments. We used a Phantom Miro 310 Lab video camera with a macro zoom lens to obtain all visual data. Single actuation events were recorded at 26,000 frames per second (fps). Estimates of time-dependent membrane volume, membrane stretch, and center displacement were calculated with custom MATLAB image analysis scripts (*SI Appendix, Experimental Image Processing*).

Actuator frequency response experiments were performed at sparking frequencies between 0.1 Hz to 1.2 kHz with 1.2 and 2 mL · min^{-1} flow rates, both at $\Phi = 0.28$. Sparks were generated with a function generator connected to an HV amplifier (TREK Model 50/12). Sparks were produced with positive-bias square waves. The spark duty cycle was increased from 0.5% to 20% to maintain spark persistence at higher frequencies. Small wires were connected to LM electrodes to reduce the electrode gap. Membrane center displacements were measured with a laser displacement sensor (LTS-050–10, MTI Instruments). Additional details are provided in *SI Appendix, Experimental Frequency Response Analysis*.

We confirmed individual actuator function by manually switching HV relay (COTO Technology) combinations, igniting all nine cylinders, recording their displacements at 10,000 fps. Both a miniature HV module (EMCO Q20-5, XP Power) and an HV amplifier (Model 50/12, TREK, Inc.) were used to generate the input breakdown voltages. An Arduino Uno was programmed to control HV relays and produce actuation sequences in the latching pin array. Tactile display demonstrations were recorded at 18,000 fps.

Simulations. The LFP model was developed in Python using Cantera version 2.4.0. The LFSI model was developed in Mathematica 12.1. Details about theory and numerics are provided in *SI Appendix, Laminar Flame Propagation Model (LFP)* and *Linearized Fluid-Structure Interaction Model (LFSI)*.

Data Availability. Raw experimental data and simulation scripts have been deposited in Figshare (https://doi.org/10.6084/m9.figshare.15169077).

ACKNOWLEDGMENTS. This work was supported in part by NSF CMMI-1537413, an Air Force Office of Scientific Research contract (FA9550-20-1-0254) and a Sloan Minority PhD Program fellowship (R.H.H.). We thank Nikolaos Bouklas and Andy Ruina for helpful discussions. We thank Patrick Wick for assistance with Schlieren imaging. We thank Kirstin Petersen for 3D printer and router access. We thank the Laboratory of Atomic and Solid State Physics (LASSP) Professional Machine Shop for experimental fabrication services. We thank Ronda Porras for providing remote work resources during the pandemic laboratory shutdown. The figure color palette was inspired by a beverage label design: © 2020 Daniella Manini.

1. A. Rizzi, *The Science Before Science* (IAP Press, 2004).
2. C. Papagno, C. Cecchetto, A. Pisoni, N. Bolognini, Deaf, blind or deaf-blind: Is touch enhanced? *Exp. Brain Res.* **234**, 627–636 (2016).
3. L. B. Merabet, A. Pascual-Leone, Neural reorganization following sensory loss: The opportunity of change. *Nat. Rev. Neurosci.* **11**, 44–52 (2010).
4. U. Proske, The role of muscle proprioceptors in human limb position sense: A hypothesis. *J. Anat.* **227**, 178–183 (2015).
5. P. Hewston, N. Deshpande, Falls and balance impairments in older adults with Type 2 diabetes: Thinking beyond diabetic peripheral neuropathy. *Can. J. Diabetes* **40**, 6–9 (2016).
6. C. Sommer *et al*., Polyneuropathies. *Dtsch. Arztebl. Int.* **115**, 83–90 (2018).
7. F. B. Axelrod, G. Gold-von Simson, Hereditary sensory and autonomic neuropathies: Types II, III, and IV. *Orphanet J. Rare Dis.* **2**, 39 (2007).
8. R. Hanewinckel, M. A. Ikram, P. A. van Doorn, "Peripheral neuropathies" in *Handbook of Clinical Neurology*, M. J. Aminoff, F. Boller, D. F. Swaab, Eds. (Elsevier B.V., 2016), pp. 263–282.
9. M. F. Bear, B. W. Connors, M. A. Paradiso, *Neuroscience: Exploring the Brain* (Wolters Kluwer, Philadelphia, PA, Fourth edition, 2015).
10. R. S. Johansson, J. R. Flanagan, Coding and use of tactile signals from the fingertips in object manipulation tasks. *Nat. Rev. Neurosci.* **10**, 345–359 (2009).
11. A. Zimmerman, L. Bai, D. D. Ginty, The gentle touch receptors of mammalian skin. *Science* **346**, 950–954 (2014).
12. M. Hollins, S. R. Risner, Evidence for the duplex theory of tactile texture perception. *Percept. Psychophys.* **62**, 695–705 (2000).
13. J. C. Makous, R. M. Friedman, C. J. Vierck Jr, A critical band filter in touch. *J. Neurosci.* **15**, 2808–2818 (1995).
14. N. Runyan, D. Blazie, *EAP Actuators Aid the Quest for the "Holy Braille" of Tactile Displays in Electroactive Polymer Actuators and Devices (EAPAD)* (SPIE, 2010), pp. 764207.
15. C. S. Haines *et al*., Artificial muscles from fishing line and sewing thread. *Science* **343**, 868–872 (2014).
16. Y. Qiu, Z. Lu, Q. Pei, Refreshable tactile display based on a bistable electroactive polymer and a stretchable serpentine joule heating electrode. *ACS Appl. Mater. Interfaces* **10**, 24807–24815 (2018).
17. J. Streque, A. Talbi, P. Pernod, V. Preobrazhensky, Pulse-driven magnetostatic microactuator array based on ultrasoft elastomeric membranes for active surface applications. *J. Micromech. Microeng.* **22**, 095020 (2012).
18. J. Li, S. Kim, J. A. Miele, M. Agrawala, S. Follmer, "Editing spatial layouts through tactile templates for people with visual impairments" in Conference on Human Factors in Computing Systems - Proceedings, (Association for Computing Machinery, Glasgow, Scotland, 2019).

19. N. Besse, S. Rosset, J. J. Zarate, H. Shea, Flexible active skin: Large reconfigurable arrays of individually addressed shape memory polymer actuators. *Adv. Mater. Technol.* **2**, 1700102 (2017).
20. X. Wu, S. H. Kim, H. Zhu, C. H. Ji, M. G. Allen, A refreshable braille cell based on pneumatic microbubble actuators. *J. Microelectromech. Syst.* **21**, 908–916 (2012).
21. X. Yu *et al*., Skin-integrated wireless haptic interfaces for virtual and augmented reality. *Nature* **575**, 473–479 (2019).
22. HaptX: Haptic gloves for virtual reality and robotics. https://haptx.com/technology/. Accessed 15 May 2021.
23. R. Heisser, *HaptX Booth Demonstration* (SOLIDWORKS World, 2019).
24. Parker Hannifin, X-Valve - Miniature Pneumatic Solenoid Valve. https://ph.parker.com/us/12051/en/x-valve-miniature-pneumatic-solenoid-valve. Accessed 24 October 2020.
25. M. A. Unger, H.-P. Chou, T. Thorsen, A. Scherer, S. R. Quake, Monolithic microfabricated valves and pumps by multilayer soft lithography. *Science* **288**, 113–116 (2000).
26. B. E. Layton, A comparison of energy densities of prevalent energy sources in units of joules per cubic meter. *Int. J. Green Energy* **5**, 438–455 (2008).
27. X. Yang, L. Chang, N. O. Pérez-Arancibia, An 88-milligram insect-scale autonomous crawling robot driven by a catalytic artificial muscle. *Sci. Robot.* **5**, 15 (2020).
28. C. M. Spadaccini *et al*., High power density silicon combustion systems for micro gas turbine engines. *J. Eng. Gas Turbine. Power* **125**, 709–719 (2003).
29. Y. Ju, K. Maruta, Microscale combustion: Technology development and fundamental research. *Pror. Energy Combust. Sci.* **37**, 669–715 (2011).
30. R. F. Shepherd *et al*., Using explosions to power a soft robot. *Angew. Chem. Int. Ed. Engl.* **52**, 2892–2896 (2013).
31. M. Wehner *et al*., An integrated design and fabrication strategy for entirely soft, autonomous robots. *Nature* **536**, 451–455 (2016).
32. C. Stergiopulos *et al*., "A soft combustion-driven pump for soft robots" in *Proceedings of the ASME 2014 Conference on Smart Materials, Adaptive Structures and Intelligent Systems*, (ASME, Newport, RI, 2014), pp. 1–6.
33. C. M. Schumacher, M. Loepfe, R. Fuhrer, R. N. Grass, W. J. Stark, 3D printed lost-wax casted soft silicone monoblocks enable heart-inspired pumping by internal combustion. *RSC Advances* **4**, 16039–16042 (2014).
34. M. T. Tolley *et al*., "An untethered jumping soft robot" in 2014 IEEE/RSJ International Conference on Intelligent Robots and Systems, Wolfram Burgard, Editor-in-Chief (IEEE, Chicago, IL 2014), pp. 561–566.
35. D. Briand *et al*., "Large deformation balloon micro-actuator based on pyrotechnics on chip" in *Proceedings of the IEEE International Conference on Micro Electro Mechanical Systems (MEMS)*, (Tucson, AZ, 2008), pp. 535–538.
36. G. Camino, S. M. Lomakin, M. Lazzari, Polydimethylsiloxane thermal degradation. Part 1. Kinetic aspects. *Polymer (Guildf.)* **42**, 2395–2402 (2001).
37. F. Ilievski, A. D. Mazzeo, R. F. Shepherd, X. Chen, G. M. Whitesides, Soft robotics for chemists. *Angew. Chem. Int. Ed. Engl.* **50**, 1890–1895 (2011).
38. M. D. Dickey, Stretchable and soft electronics using liquid metals. *Adv. Mater.* **29**, 1606425 (2017).
39. J. B. Heywood, *Internal Combustion Engine Fundamentals* (McGraw-Hill Education, ed. 1, 1988).
40. S. R. Turns, *An Introduction to Combustion: Concepts and Applications* (McGraw-Hill Education, ed. 3, 2011).
41. R. Long, K. R. Shull, C. Y. Hui, Large deformation adhesive contact mechanics of circular membranes with a flat rigid substrate. *J. Mech. Phys. Solids* **58**, 1225–1242 (2010).
42. A. L. Flory, D. A. Brass, K. R. Shull, Deformation and adhesive contact of elastomeric membranes. *J. Polym. Sci., B, Polym. Phys.* **45**, 3361–3374 (2007).
43. R. Long, C. Y. Hui, Axisymmetric membrane in adhesive contact with rigid substrates: Analytical solutions under large deformation. *Int. J. Solids Struct.* **49**, 672–683 (2012).
44. P. Chakraborti *et al*., A compact dielectric elastomer tubular actuator for refreshable Braille displays. *Sens. Actuators A Phys.* **179**, 151–157 (2012).
45. Y. Kato *et al*., Sheet-type braille displays by integrating organic field-effect transistors and polymeric actuators. *IEEE Trans. Electron Dev.* **54**, 202–209 (2007).
46. I. M. Koo *et al*., Development of soft-actuator-based wearable tactile display. *IEEE Trans. Robot.* **24**, 549–558 (2008).
47. S. Gallo, C. Son, H. J. Lee, H. Bleuler, I. J. Cho, A flexible multimodal tactile display for delivering shape and material information. *Sens. Actuators A Phys.* **236**, 180–189 (2015).
48. A. N. Tiwari, M. Rajput, N. A. Chien, N. Mathews, Highly transparent and integrable surface texture change device for localized tactile feedback. *Small* **14**, 1702312 (2018).
49. G. Bubak, A. Ansaldo, L. Ceseracciu, K. Hata, D. Ricci, *Bucky Gel Actuators Optimization Towards Haptic Applications in Electroactive Polymer Actuators and Devices (EAPAD)* (SPIE, 2014), pp. 905611.
50. H. Zhao *et al*., Compact dielectric elastomer linear actuators. *Adv. Funct. Mater.* **28**, 1804328 (2018).
51. R. Velázquez, E. Pissaloux, M. Hafez, J. Szewczyk, *A Low-Cost Highly-Portable Tactile Display Based on Shape Memory Alloy Micro-Actuators* (IEEE, 2005).
52. E. Strasnick, S. Follmer, "Applications of switchable permanent magnetic actuators in shape change and tactile display" in UIST 2016 Adjunct - Proceedings of the 29th Annual Symposium on User Interface Software and Technology, (Association for Computing Machinery, Inc., Tokyo, Japan, 2016), pp. 123–125.
53. J. Kim *et al*., Braille display for portable device using flip-latch structured electromagnetic actuator. *IEEE Trans. Haptics* **13**, 59–65 (2020).
54. A. K. Han, S. Ji, D. Wang, M. R. Cutkosky, Haptic surface display based on miniature dielectric fluid transducers. *IEEE Robot. Autom. Lett.* **5**, 4021–4027 (2020).
55. E. Leroy, R. Hinchet, H. Shea, Multimode hydraulically amplified electrostatic actuators for wearable haptics. *Adv. Mater.* **32**, e2002564 (2020).
56. J. J. Zarate, O. Gudozhnik, A. S. Ruch, H. Shea, "Keep in touch: Portable haptic display with 192 high speed taxels" in *Conference on Human Factors in Computing Systems - Proceedings*, (Association for Computing Machinery, Denver, CO, 2017), pp. 349–352.
57. R. J. Wood, E. Steltz, R. S. Fearing, Optimal energy density piezoelectric bending actuators. *Sens. Actuators A Phys.* **119**, 476–488 (2005).
58. X. Ji *et al*., Untethered feel-through haptics using 18-μm thick dielectric elastomer actuators. *Adv. Funct. Mater.* 10.1002/adfm.202006639 (2020).
59. H. Phung *et al*., Tactile display with rigid coupling based on soft actuator. *Meccanica* **50**, 2825–2837 (2015).
60. N. Torras *et al*., Tactile device based on opto-mechanical actuation of liquid crystal elastomers. *Sens. Actuators A Phys.* **208**, 104–112 (2014).
61. D. G. Goodwin, R. L. Speth, H. K. Moffat, Cantera: An object-oriented software toolkit for chemical kinetics, thermodynamics, and transport processes. https://www.cantera.org. Version 2.5.1. (2021). 10.5281/zenodo.4527812.
62. E. S. Oran, V. N. Gamezo, Origins of the deflagration-to-detonation transition in gas-phase combustion. *Combust. Flame* **148**, 4–47 (2007).
63. V. Bychkov, V. Akkerman, G. Fru, A. Petchenko, L.-E. Eriksson, Flame acceleration in the early stages of burning in tubes. *Combust. Flame* **150**, 263–276 (2007).
64. W. Han, Y. Gao, C. K. Law, Flame acceleration and deflagration-to-detonation transition in micro- and macro-channels: An integrated mechanistic study. *Combust. Flame* **176**, 285–298 (2017).
65. J. D. Ott, E. S. Oran, J. D. Anderson, A mechanism for flame acceleration in narrow tubes. *AIAA J.* **41**, 1391–1396 (2003).
66. M. H. Wu, M. P. Burke, S. F. Son, R. A. Yetter, Flame acceleration and the transition to detonation of stoichiometric ethylene/oxygen in microscale tubes. *Proc. Combust. Inst.* **31**, 2429–2436 (2007).
67. J. Koch, M. Kurosaka, C. Knowlen, J. N. Kutz, Mode-locked rotating detonation waves: Experiments and a model equation. *Phys. Rev. E* **101**, 013106 (2020).
68. I. Humphry Davy, On the fire-damp of coal mines, and on methods of lighting the mines so as to prevent its explosion. *Philos. Trans. R. Soc. Lond.* **106**, 1–22 (1816).
69. V. S. Babkin, *Prevention of Hazardous Fires and Explosions* (Springer-Science+Business Media, 1st ed., 1999).
70. J. Y. Tsao *et al*., Ultrawide-bandgap semiconductors: Research opportunities and challenges. *Adv. Electron. Mater.* **4**, 1600501 (2018).
71. K. Tetzner *et al*., Lateral 1.8 kV β-Ga 2 O 3 MOSFET with 155 MW/cm 2 power figure of merit. *IEEE Electron Device Lett.* **40**, 1503–1506 (2019).
72. D. Ni, B. Davaji, R. Shepherd, A. Lal, "3D printed pyroelectric lithium-niobate high voltages source with pull-in regulated output" in 2020 IEEE 33rd International Conference on Micro Electro Mechanical Systems (MEMS, Vancouver, BC, Canada, 2020), pp. 586–589.
73. G. Liu *et al*., Self-gauged fiber-optic micro-heater with an operation temperature above 1000°C. *Opt. Lett.* **42**, 1412–1415 (2017).
74. S. T. Weir, D. D. Jackson, S. Falabella, G. Samudrala, Y. K. Vohra, An electrical microheater technique for high-pressure and high-temperature diamond anvil cell experiments. *Rev. Sci. Instrum.* **80**, 013905 (2009).
75. M. J. Schonhuber, Breakdown of gases below Paschen minimum: Basic design data of high-voltage equipment. *IEEE Trans. Power Apparatus Syst* **PAS-88**, 100–107 (1969).
76. B. W. Ward, T. J. Lewis, "The electric strength and conduction of methane gas at high pressures" in Annual Report 1963 Conference on Electrical Insulation (IEEE, White Sulphur Springs, WV, 1963).
77. D. G. Logan, J. Pentzer, S. N. Brennan, K. Reichard, Comparing batteries to generators as power sources for use with mobile robotics. *J. Power Sources* **212**, 130–138 (2012).
78. G. R. Schmidt, H. P. Gerrish, J. J. Martin, G. A. Smith, K. J. Meyer, Antimatter requirements and energy costs for near-term propulsion applications. *J. Propuls. Power* **16**, 923–928 (2000).
79. D. Ferreira, M. Boaventura, P. Bárcia, R. D. Whitley, A. Mendes, Two-stage vacuum pressure swing adsorption using AgLiLSX zeolite for producing 99.5+% oxygen from air. *Ind. Eng. Chem. Res.* **55**, 722–736 (2016).
80. S. Saxena, L. Kong, M. G. Pecht, Exploding e-cigarettes: A battery safety issue. *IEEE Access* **6**, 21442–21466 (2018).
81. C. Larson *et al*., Highly stretchable electroluminescent skin for optical signaling and tactile sensing. *Science* **351**, 1071–1074 (2016).
82. K. L. Dorsey, N. Lazarus, Lifetime of liquid metal wires for stretchable devices. *Adv. Mater. Technol.* **6**, 2001100 (2021).